Analysis of gravity waves in the tropical middle atmosphere over La Reunion Island (21°S, 55°E) with lidar using wavelet techniques

Fabrice Chane-Ming, Franck Molinaro, Jean Leveau, Philippe Keckhut, Alain Hauchecorne

Ann. Geophysicae 18, 485–498 (2000) © EGS – Springer-Verlag 2000

Annales Geophysicae

Analysis of gravity waves in the tropical middle atmosphere over La Reunion Island (21°S, 55°E) with lidar using wavelet techniques

F. Chane-Ming[1], **F. Molinaro**[1], **J. Leveau**[1], **P. Keckhut**[2], **A. Hauchecorne**[2]

[1] Laboratoire de Physique de l'Atmosphère, Université de la Réunion, Faculté des Sciences et Technologies, 15 Av. René Cassin, BP 7151, 97715 Saint Denis Cedex 9, France. E-mail: fchane@univ-reunion.fr
[2] Service d'Aéronomie du CNRS, BP 3, 91371 Verrières-Le-Buisson Cedex 3 Paris, France

Received: 28 May 1999 / Revised: 5 January 2000 / Accepted: 12 January 2000

Abstract. The capabilities of the continuous wavelet transform (CWT) and the multiresolution analysis (MRA) are presented in this work to measure vertical gravity wave characteristics. Wave properties are extracted from the first data set of Rayleigh lidar obtained between heights of 30 km and 60 km over La Reunion Island (21°S, 55°E) during the Austral winter in 1994 under subtropical conditions. The altitude-wavelength representations deduced from these methods provide information on the time and spatial evolution of the wave parameters of the observed dominant modes in vertical profiles such as the vertical wavelengths, the vertical phase speeds, the amplitudes of temperature perturbations and the distribution of wave energy. The spectra derived from measurements show the presence of localized quasi-monochromatic structures with vertical wavelengths < 10 km. Three methods based on the wavelet techniques show evidence of a downward phase progression. A first climatology of the dominant modes observed during the Austral winter period reveals a dominant night activity of 2 or 3 quasi-monochromatic structures with vertical wavelengths between 1–2 km from the stratopause, 3–4 km and 6–10 km observed between heights of 30 km and 60 km. In addition, it reveals a dominant activity of modes with a vertical phase speed of −0.3 m/s and observed periods peaking at 3–4 h and 9 h. The characteristics of averaged vertical wavelengths appear to be similar to those observed during winter in the southern equatorial region and in the Northern Hemisphere at mid-latitudes.

Key words: Meteorology and atmospheric dynamics (climatology; middle atmosphere dynamics; waves and tides)

Correspondence to: F. Chane-Ming

1 Introduction

Hines (1960) first suggested that irregular motions observed in the upper atmosphere might be interpreted in terms of internal gravity waves. Gravity wave processes are now recognized to be important for the dynamics of the atmosphere (Holton, 1975; Andrews *et al.*, 1987). Small-scale waves such as gravity waves cannot be directly resolved in the major existing atmospheric general circulation models and therefore they have to be parametrized (McLandress, 1998). With recent computer capabilities together with development in GCM, resolving gravity waves explicitly with higher vertical resolution is becoming possible and now seems to provide realistic global characteristics of gravity waves (Sato *et al.*, 1999). However, local and global observations with high resolution are needed to improve our understanding of the processes associated with gravity wave motions. This knowledge is required to provide more realistic integration of these processes in numerical models and their effects on the global circulation to account for potential climate change. A wide variety of in situ and remote sensing techniques has now provided numerous observational data in the middle atmosphere of the Northern Hemisphere. The data from meteorological rocketsonde and high-resolution radiosonde observations enabled Hirota (1984), Hamilton (1991), Eckermann *et al.* (1995) and Allen Vincent (1995) to draw up a climatology of gravity waves in the middle and the lower atmosphere. However these techniques do not provide suitable measurements for the study of the high time evolution of gravity wave processes. Recent works on the characteristics of gravity wave parameters, wave spectra and the temporal evolution are mainly based on techniques such as radar (Nakamura *et al.*, 1993; Kuo and Lue, 1994; Connor and Avery, 1996). Unlike radar which can not provide information in the upper part of the stratosphere, lidar techniques provide suitable measurements with high spatial and temporal resolution for the study of gravity

waves at heights between 30 km and 80 km using a Rayleigh lidar (Chanin and Hauchecorne, 1981; Shibata *et al.*, 1986), between 10 km and 30 km using a Raman lidar (Keckhut *et al.*, 1990; Hauchecorne *et al.*, 1992) and at heights 85–105 km using a Na lidar (Gardner and Voelz, 1987). Continuous measurements with a high time and spatial resolution are provided by these instruments and enable one to study day-to-day variability of gravity waves related to the wave propagation, the wave-wave and wave-mean flow interactions over an arbitrary time scales, the activity of wave sources, and the climatological variability.

Gravity wave variances as a function of altitude, season and latitude are now well understood at mid-latitude continental observations (Eckermann, 1995a; Alexander, 1998). However, due to sparse observational data in the Southern Hemisphere, more particularly in the tropics, the understanding of gravity wave processes and their effects still remains incomplete. The time and spatial localization of gravity waves, their characteristics and the activity are poorly documented (Vincent, 1984, 1990). Comparisons with the Northern Hemisphere have shown some similar characteristics (Fritts, 1990). Tsuda *et al.* (1994) argued that similar atmospheric background conditions might explain this similarity in the observations. However, differences of the source distribution and the strength at the lower levels are expected due to hemispheric differences. Maps of gravity wave variance extrapolated from the Microwave Limb Sounder (MLS) data at heights between 33 km and 80 km show large amplitudes associated with subtropical land masses and the tropospheric cumulus convection in the summer hemisphere and with the activity of the subtropical jet in the winter hemisphere (Wu and Waters, 1997). The increasing gravity wave variance above the stratopause and the enhancement above Madagascar and its surroundings are observed (Wu and Waters, 1997). Many of the geographical features in these MLS variance maps were recently reinterpreted by Alexander (1998) in light of the observational filters and wave refraction by the background wind and not in terms of geographical variations in gravity wave activity. Nevertheless the tropospheric cumulus convection, the surface topography and the subtropical jet are well-assumed to be the major sources of gravity wave energy in the middle atmosphere over the southwest Indian Ocean.

Adapted tools are required to extract the proper information from the measurements. The Fourier transform remains most often used for the study of gravity waves although this technique is adapted to stationary signals and only retrieves the spectral information. The time and spatial localization is also essential information for gravity waves. The time-frequency techniques provide a compromise between time (or spatial) and frequency information through the well-known Heisenberg uncertainty relation of digital signal processing. In the particular case of the wavelet analysis, we choose a localized set of orthogonal basis functions which looks like the structures that we want to analyze. Then, this pattern is dilated and moves along the signal to capture similar structures inside the signal. Therefore, this last method is well-adapted to the analysis of localized multi-scaled wavelike structures such as gravity waves of which the amplitude and the phase vary in time and in space (Sato and Yamada, 1994; Tannhauser and Attié, 1995; Bacmeister *et al.*, 1996; Demoz *et al.*, 1998).

In this study, we apply wavelet techniques to vertical lidar temperature profiles to characterize quasi-monochromatic structures (Gill, 1982; Gardner *et al.*, 1989) associated with gravity waves in the middle atmosphere. We focus our attention on some gravity wave characteristics observed in the upper stratosphere and the lower mesosphere between heights of 30 km and 60 km from the first measurements obtained in 1994 with a Rayleigh lidar at La Reunion Island (21°S, 55°E) which is located in the southern subtropics (2510 km^2; 690 km east from Madagascar) (refer to maps of Barcelo *et al.*, 1997). First, lidar data obtained at La Reunion Island are presented. Then, applications of the continuous wavelet transform (CWT) and the multiresolution analysis (MRA) on lidar data are examined. The time and spatial evolution of certain gravity wave parameters is illustrated with a typical night of observation. The observed vertical phase progression is analyzed by three complementary methods derived from wavelet techniques. Finally we present preliminary climatology for the first year.

2 Experimental data

A Rayleigh lidar system was installed at the 'Laboratoire de Physique de l'Atmosphère' located in the north of La Reunion Island in May 1994. It is equipped with a Nd-Yag^{3+} laser source which emits 300 mJ light pulses of 10 ns duration and 532 nm wavelength upwards into the atmosphere. The characteristics of the lidar system in 1994 are summarized in Table 1. Backscattered photons are collected by a telescope with mirror areas of 0.67 m^2. By assuming that the atmosphere is an ideal gas in hydrostatic equilibrium and free of aerosols, vertical temperature profiles can then be computed with the help of the COSPAR International Reference Atmosphere (CIRA86) standard model of the atmosphere only for the initialization at the top level (Hauchecorne and Chanin, 1980; Keckhut *et al.*, 1993). The inaccuracy of mesospheric temperatures in CIRA86 particularly in the Southern Hemisphere introduces negligible errors once it is hydrostatically integrated using lidar data. The initial spatial and temporal resolution is 150 m and 15 min for the system implemented at La Reunion Island.

Table 1. Lidar characteristics in late 1994

Emission		Reception	
Laser	Nd-YAG	Area	0.67 m^2
Wavelength	532 nm	Resolution	150 m
Pulse energy	300 mJ	Detection mode	Photo-counting
Emission rate	10 Hz	Field of view	3 E-4 rad

This lidar was first developed for the stratospheric monitoring on a long term basis in framework of the Network of Detection of Stratospheric Changes (NDSC) implemented in 1991 (Kurylo and Solomon, 1990). Comparisons of vertical temperature profiles obtained at La Reunion Island with data from the Solar Mesospheric Explorer (SME) and from the National Meterological Centre (NMC) allowed the first validation of the lidar measurements (Bencherif *et al.*, 1996). The temperature fluctuations observed on the raw vertical temperature profiles from the upper stratosphere to the lower mesosphere (at heights between 30 and 60 km) are mostly associated with gravity wave motions (Chanin and Hauchecorne, 1981; Shibata *et al.*, 1986; Gardner and Voelz, 1987; Wilson *et al.*, 1991; Carswell *et al.*, 1991). Statistical errors in temperature related to photon noise are one of the key parameters that determines the suitability of these data for gravity wave studies. Time and vertical integration of vertical profiles for a night of observation with respective values 30 min and 300 m have a relative uncertainty in temperature of 0.17% at 30 km and 0.86% at 55 km, as derived from values obtained by Wilson *et al.* (1991) with a similar instrument. The vertical temperature profiles on which this study is based have 300-m vertical spatial resolution and are drawn from a 30 min time integration. These resolutions enable the study of gravity waves at heights between 30 and 60 km (Wilson *et al.*, 1991). The gravity wave signatures are extracted by subtracting the mean vertical profile from the raw vertical temperature profile. We calculate the mean temperature profile by applying a digital RII Butterworth low-pass filter (Ambardar, 1995; The MathWorks, 1998) with a cutoff of 12 km vertical wavelength λ_z. Thus we limit the vertical wavelength space to the gravity wave field with vertical wavelengths ranged from 0.6 km to 12 km. Figure 1 represents a typical vertical temperature profile obtained at heights between 30 and 60 km on the night of June 21 in 1994 during the Austral winter. The vertical temperature profiles used in this study are derived from the first lidar measurements from late May to late November in 1994.

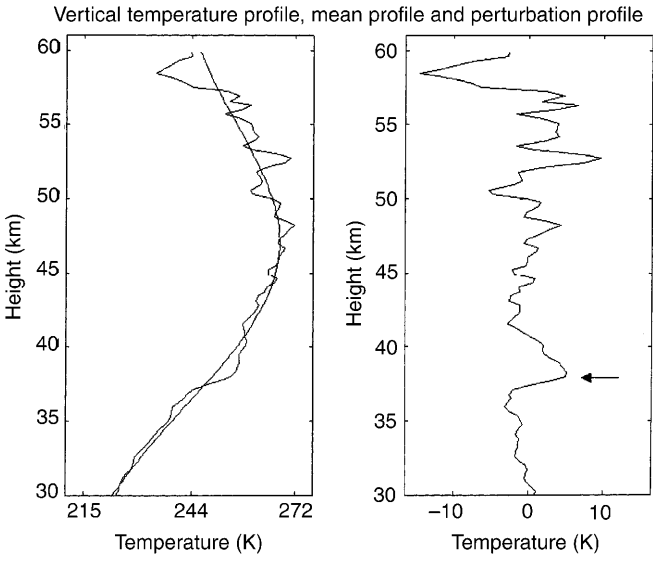

Fig. 1. Averaged vertical temperature profiles over twelve 30-min integrated profiles with 300-m spatial resolution obtained from Rayleigh lidar measurements on June 21, 1994, from 30 km to 60 km height. Raw profile, mean profile resulting from the application of a low-pass filter with a cutoff of 12-km vertical wavelength (*left panel*) and perturbation profile (*right panel*). The *arrow* indicates the location of enhancement of the original wave amplitude

3 Wavelet techniques

3.1 The continuous wavelet transform (CWT)

The CWT method consists in replacing the sinusoidal functions in the Fourier basis by a set of functions drawn from the translation and the dilation of an analyzing or 'mother' wavelet. The matching of these functions and the analyzed signal is expressed by large CWT coefficients. In this study, time scale representations are obtained by using the Morlet wavelet (Fig. 2a) and the eighth derivative of the Gaussian (Fig. 2b). These oscillating wavelets are both localized in time and frequency and well-adapted to the study of scale structures associated with gravity waves (Chane-Ming *et al.*, 1997a, b, 1998). Gaussian type wavelets and their derivatives are non-orthogonal wavelets with interesting mathematical properties (Grossmann, 1988; Farge, 1992). They are very smooth and oscillate more and more as the order of their derivatives increases.

The progressive Morlet complex-valued wavelet is commonly used in geophysics and provides separately information on the energy density and the phase of the analyzed signal (Torrence and Compo, 1998). The quadrature phase shift between the real and the imaginary parts of the Morlet complex-valued wavelet eliminates the oscillations of the wavelet in the time-scale plane. The property of progressiveness (null components for negative frequencies) of the Morlet analyzing wavelet is here useful in studying the phase progression of the CWT coefficients. It reveals that the phase has a linear progression with a 2π period for monochromatic waves (Torrésani, 1995).

The eighth derivative of the Gaussian is a real symmetrical wavelet. Real wavelets enable one to gather information on both the amplitude and phase in the same time scale plane which therefore contains more detailed structures. The eighth derivative of the Gaussian has eight vanishing moments which make the wavelet blind to patterns of nth order polynomial with $n < 8$ (Grossmann, 1988; Daubechies, 1990). Thus the analysis of such structures provides null CWT coefficients. Appendix A details some information on the computation of the CWT with the analyzing wavelets used in this work.

The time and frequency parameters are here replaced by the altitude and vertical wavelength parameters that are used in Appendix A and it results altitude-wavelength diagrams.

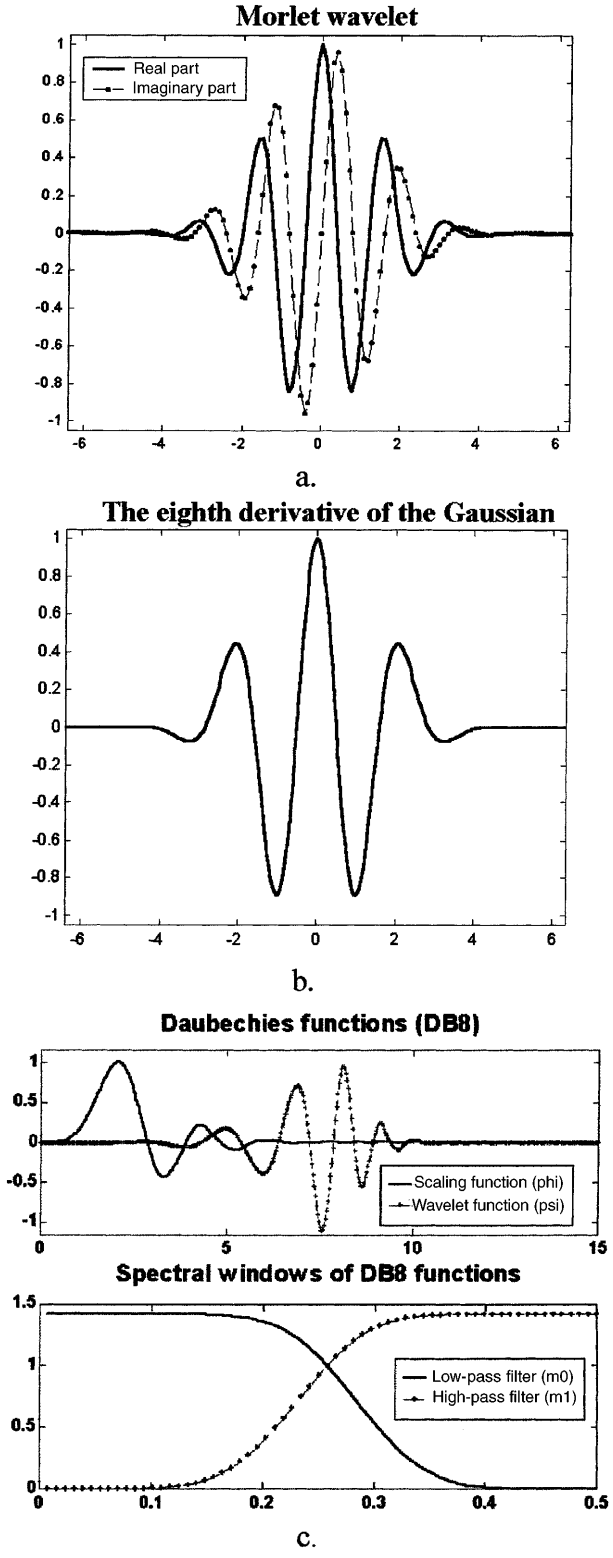

Fig. 2a–c. Analyzing wavelets used in the CWT and the multiresolution analysis: **a** the Morlet complex-valued wavelet; **b** the eighth derivative of the Gaussian; **c** the eighth order Daubechies functions: the 'scaling and wavelet functions' (*upper panel*), and corresponding spectral windows (*lower panel*)

3.2 The multiresolution analysis (MRA)

This method views the orthonormal wavelet decomposition as the application of a specific filter bank which is constituted by a set of iterated filters regularly spaced over the frequency space into octave bands (Strang and Nguyen, 1996). As with the CWT, the signal is successively broken down into different scales. The orthonormal filters are designed to solve the problem of the perfect reconstruction (the errors of reconstruction between the original signal and the reconstructed one which is produced by the MRA are negligible) and to avoid redundancies (Daubechies, 1992). Unlike the continuous wavelet analysis, a pair of filters (a low-pass and a high-pass filter) is needed at each scale level. These filters play the same role as a pair of analyzing wavelets (Fig. 2c) known as the 'scaling and wavelet functions' comparable to the CWT. The main advantages of the multiresolution analysis are that the design of filters with particular mathematical properties and their practical use are well-known. Using filter coefficients instead of analyzing wavelets allows the reduction of the computation time. The MRA is fastly implemented according to a pyramid scheme (Rioul and Vetterly, 1991).

The original signal $x(n)$ is successively decomposed into approximations $a(n)$ and details $d(n)$ (using a low-pass and a high-pass filters respectively) corresponding to successive vertical wavelength bandwidths. The fine elements (the details) included in the signal are successively retrieved from the signal so that the remaining signal (the approximation) becomes coarser and coarser after each iteration. The signal can be perfectly reconstructed by adding the details and the last approximation of the signal:

$$x(n) \approx d_1(n) + \cdots + d_i(n) + a_i(n) \ , \qquad (1)$$

where i is the i^{th} order of the iteration and n the nth element in the data series. The Daubechies wavelet with eight vanishing moments (DB8) is used in our work (Fig. 2c). The filter coefficients and their properties are reported in the texts of Daubechies (1992) and Strang and Nguyen (1996). This wavelet turns out to be smooth enough, as Gaussian wavelets are, to expand vertical temperature perturbation profiles associated with gravity wave structures.

The MRA algorithm and the DB8 coefficients are detailed in Appendix B.

4 Wavelet analysis of lidar data

4.1 Determination of vertical wavelengths

The first step of our study consists in computing the CWT of mean vertical temperature perturbation profiles. The mean vertical temperature profile is the averaged profile of 30-min integrated vertical temperature perturbation profiles obtained during a night of observation. In this way, the energy localization and the behavior of multiscaled structures can be viewed graphically. The mean temperature perturbation profile

is an average of vertical temperature fluctuation profiles during a night observation between heights of 30 and 60 km. This implies that gravity waves with short periods are filtered out. The CWT is then applied to the resulting vertical temperature perturbation profile. The CWT amplitude is here computed with the use of the Morlet wavelet depicted on an altitude-wavelength diagram (Fig. 3a). Due to the relative uncertainty in the temperature, the CWT amplitudes >3.6 are here considered meaningful at heights between 30 km and 60 km which correspond to temperature perturbation values >1 K. The normalized power spectral density computed by the standard Fourier transform on the top panel reveals the presence of two dominant structures with vertical wavelength bandwidths of 2–4 km and 6–11 km. The representation of vertical wavelengths as a function of altitude clearly shows what happens in the upper stratosphere, the stratopause region and the lower mesosphere. It reveals that the temperature perturbation profiles are made up of the superposition of different structures. Two dominant structures of approximately 2–4 km and 6–11 km vertical wavelengths are brought

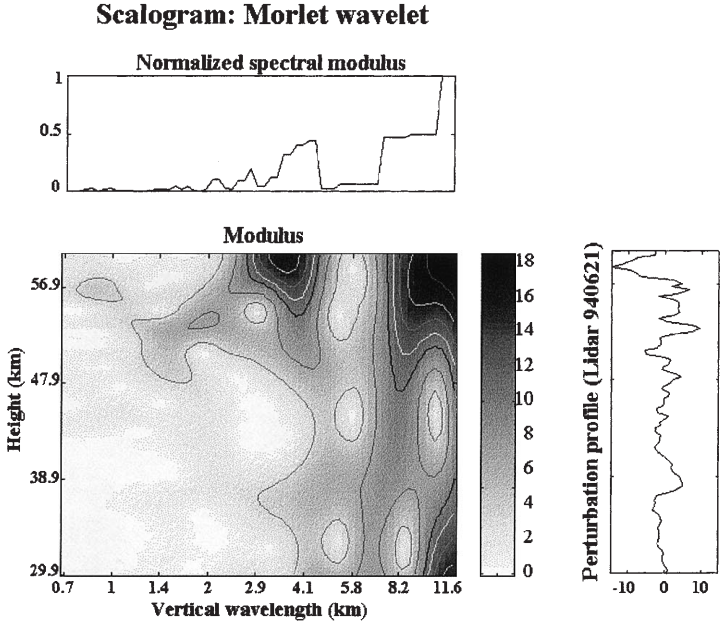

a.

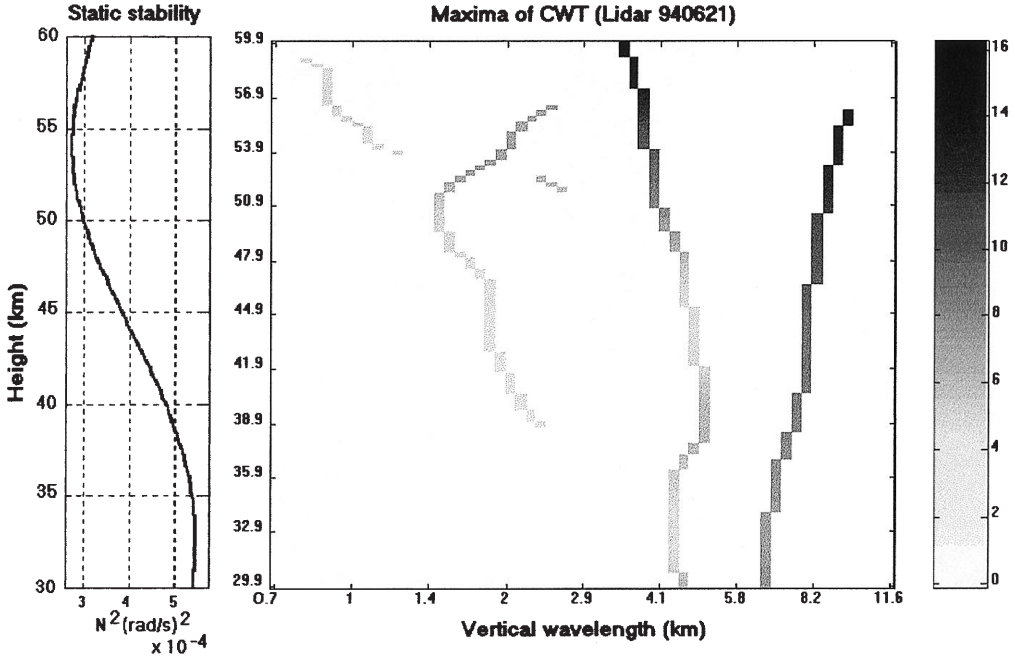

b.

Fig. 3a, b. Averaged vertical temperature profiles over twelve 30-min integrated profiles with a 300-m spatial resolution obtained from Rayleigh lidar measurements on June 21, 1994, between heights of 30 km and 60 km. **a** The CWT representation using the Morlet wavelet of the averaged vertical temperature perturbation profile (*right panel*). The normalized power spectral density with the standard FFT analysis is seen on the *top panel*. The CWT amplitude yields information on the spatial distribution and the evolution of different events in the signal. **b** Skeleton of the CWT is extracted from the CWT amplitude. The static stability is plotted on the *left panel*. Three localized dominant quasi-monochromatic structures are present with 1.5–2 km, 3.5–5 km and 6.2–9.7 km vertical wavelengths

into view. The intensity distribution of the CWT amplitude shows a clear increase of wave amplitudes in the lower mesosphere which is attributed to the decrease in the atmospheric gas density with the increasing altitude. To extract information quickly from the CWT, a method exists of reducing the CWT to its 'skeleton' (Torrésani, 1995). The essential information of the signal is expressed in the spectral lines describing the amplitudes and the instant frequencies of wavelike structures. The spectral lines provided by the CWT maxima with values $>10\%$ of the maximum value are plotted in Fig. 3b. The values of the static stability on the left panel enable us to identify the different regions at heights between 30 and 60 km: the upper stratosphere (30–40 km), the stratopause (40–50 km) and the lower mesosphere (50–60 km). The figure shows evidence of three dominant quasi-monochromatic waves with vertical wavelengths λ_z between 1.5–2 km above the stratopause, 3.5–5 km and 6.2–9.7 km over the whole altitude range. The static stability N^2 as a function of altitude gives values of 5×10^{-4} and 3×10^{-4} $(\mathrm{rad/s})^2$ in the upper stratosphere and the lower mesosphere respectively and follows a linear trend between these values through the stratopause.

For the case presented here, the spectral line evolution for both longer wavelike patterns (λ_v = 3.5–5 km and 6.2–9.7 km) is steady in the upper stratosphere to 36 km in altitude from where the static stability begins to decrease. The long vertical wavelength increases from the upper stratosphere (λ_{v1} = 6.2 km) to the lower mesosphere (λ_{v2} = 9.7 km) with a ratio of 1.56 ($\lambda_{v2}/\lambda_{v1}$) as the static stability decreases with a ratio of 1.44 (N_1/N_2). The evolution of the static stability and the vertical wavelength with altitude can be explained by the hydrostatic linear wave dispersion relation. The simplified hydrostatic dispersion relation ($m = \pm\frac{N}{\omega}k_h$) shows that the vertical wave number (m) is proportional to the static stability (N) by assuming that the ratio of the horizontal wavenumber and the intrinsic frequency remains constant. In contrast, the decrease of both the shorter vertical wavelengths from the stratopause might suggest an important role of wave processes such as the wave absorption and the dissipation of wave energy due to the wind filtering by the mean background zonal flow governed by the mid-latitude westerlies in June 1994 at the stratopause level (Fig. 4). This hypothesis is reinforced by the fact that gravity waves with short vertical wavelengths have small intrinsic phase speeds and therefore they are more affected by the effects of gradients of wind, filtering and dissipation. In fact as $c_x - \bar{u}$ decreases, the vertical wavelength is shortened. In the limit case as $c_x = \bar{u}$, the wave may encounters critical levels where the wave energy is absorbed by the mean flow (Lindzen, 1981). A fuller discussion of the role of background wind variations on gravity variances and vertical wavelengths measured by vertical profilers with height has been given by Eckermann (1995a, b), Eckermann *et al.* (1995) and Alexander (1998). The vertical wavelength does vary with the background wind speed depending on the azimuth angle between the wind and wave-propagation vectors (refer to Fig. 4 of Eckermann *et al.*, 1995). If waves are coaligned with the wind then this can produce large wavelength changes which can actually shift waves to wavelengths that become too large or too short for lidar to measure. Thus large observed values λ_v, from the stratopause in winter, are consistent with the increase of the mean wind speeds with height. The stratopause clearly appears as a transitional region affecting wavelike structures. Moreover, partial wave reflection and/or refraction may occur at the boundaries of the stratopause characterized by discontinuities of the static stability. Such wave phenomena are expected when N^2 decreases at greater heights. In particular, the waves with a short horizontal wavelength encounter turning levels during winter at different altitudes with an increasing horizontal wavelength (Salby, 1995). The increase of wave amplitude at 38 km in altitude (indicated by an arrow on right panel of Fig. 1) located at the lower border of the stratopause is well marked in the vertical profile of temperature perturbations and suggests an enhancement of the original wave amplitude at this altitude. Gradients in background temperature and in the wind field might induce wave reflection and ducted mode waves (Isler *et al.*, 1997). The nonlinear interactions between both the longer waves in a shear flow (Vanneste and Vial, 1997) might provide some possible explanation of the existence of waves with short vertical wavelengths of about 2 km above the stratopause.

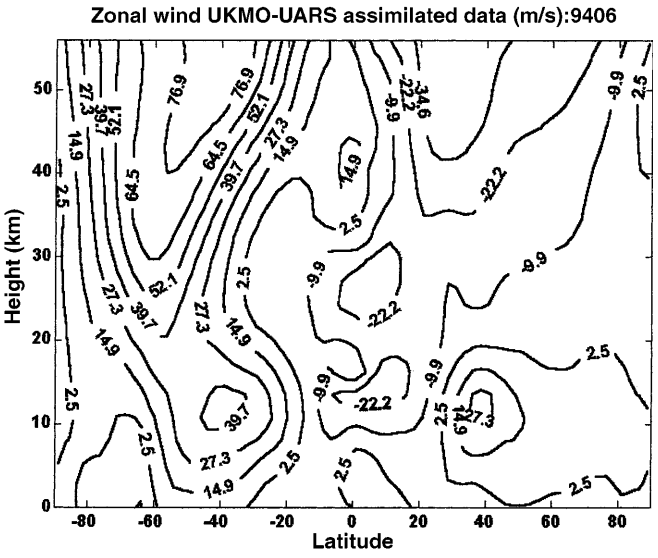

Fig. 4. Latitude-height section of zonal wind profile of June 1994 based on UKMO-UARS assimilated data

The CWT of night averaged vertical temperature perturbation profiles expresses the mean behavior of observed structures during a night. It highlights locations where structures are often confined and/or where important events occur. However transient events with short periods are erased. Therefore the analysis favors the detection of gravity-waves with long periods. We cannot assert the simultaneous presence of the different observed waves or the existence of an interaction between the observed modes. The CWT applied to

successive 30 min integrated vertical temperature perturbation profiles enables us to observe the time evolution of vertical wavelengths during a night (Chane-Ming, 1998).

4.2 Determination of the phase progression

The phase progression of the gravity wave is generally deduced directly from vertical profiles filtered around the studied wavelength (Gardner *et al.*, 1989). In this section, three new and complementary methods of the phase estimation based on the time scale analysis are illustrated on the same night of observation on June 21, 1994.

The first method relies upon the property of progressiveness of the Morlet complex-valued wavelet. The phase progression of monochromatic structures is linear and 2π periodic. These can be seen on 30 min average profiles for this night, for example on the sixth and the ninth 30 min average profiles (hereafter referred to as numbers 6 and 9). Phase sections for these structures are displayed in Fig. 5. The superposition of the phase for both vertical perturbation profiles shows an evident downward phase progression for the wavelike structures with 7 km vertical wavelength. The lapse between both 30 min average profiles enables us to easily estimate a vertical phase speed c_z of -0.25 m/s at 47 km in altitude.

The second method takes the variation of vertical wavelengths into account. The eighth derivative of the Gaussian is used to locate amplitude extrema of wavelike structures. The shape in the CWT representation of the extrema enables us to trace the time and spatial progression of the maxima and the minima on the successive 30 min average profiles. The contour lines of the positive and negative real part of the CWT coefficients are deduced from the 30 min average profiles

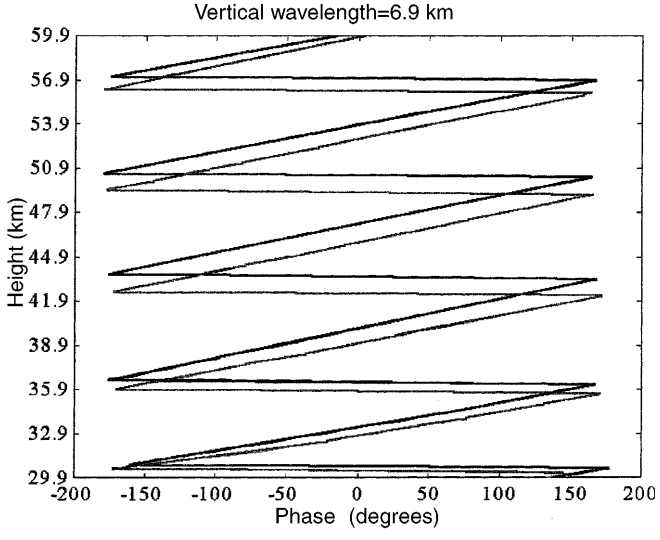

Fig. 5. Phase sections obtained by the application of the Morlet wavelet on file numbers 6 and 9 on June 21, 1994, (*black* and *gray curves* respectively) are plotted for the dominant quasi-monochromatic waves with 6.9 km vertical wavelengths. A clear downward phase progression is observed

numbers 6 and 9. They are superposed in Fig. 6a, b. Figure 6c, d shows zoom-ins on these patterns respectively in the mesosphere for the short vertical wavelength wave and between heights of 30 km and 60 km for the long vertical wavelength wave. Almost all patterns here can be identified in both 30 min average profiles. These patterns have an evident downward progression indicated by the direction of the arrows. The vertical wavelengths vary with time and location and thus the estimation of phase progression depends on the wave stability. This method becomes rather difficult to apply when the patterns cannot be identified on the successive 30 min average profiles. The vertical phase speed is estimated at -0.26 m/s in the stratopause for the mode with 7 km vertical wavelength (Fig. 6d).

For both these methods, we use two 30 min average profiles which have similar characteristics and whose patterns are easily identified. In this next and last method, wavelike structures are extracted by the MRA from the successive 30 min average profiles of the night observation. Twelve vertical profiles are obtained for the night of June 21 over 6 h of experimentation. Figure 7 shows the evolution of successive details $d_4(z)$ for the long wave of 7 km vertical wavelength observed in all 30 min average profiles during this night. The progression of maximum and minimum amplitudes shows evidence of a downward phase progression at the altitudes ranging from 45 km to 55 km as expected for long period gravity waves (downward phase progression corresponds to upward wave energy propagation). Using 30 min average profiles numbers 6 and 9, we estimate a mean value of about -0.23 m/s between heights of 40 and 50 km. From the 30 min average profile of numbers 7 to 12, a clear larger downward phase progression is observed. In the upper stratosphere, no true phase progression is observed. This method provides a global view on the phase speed trend. This method is similar to the classical method which is used to analyze time evolution of gravity wave motions with the difference that quasi-monochromatic structures are retrieved by orthogonal filters without sidelobe effects of the spectral windows in the present method.

The phase speed values are plotted in Fig. 8a, b for the first two methods. A comparison between these methods is depicted from 30 min average profiles numbers 6 and 9. The results of the first method are similar to those obtained by the second one in the region where the vertical wavelength varies slowly with height. A phase speed minimum of -0.26 m/s is located in the stratopause region at about 47 km for the 7 km vertical wavelength wave. The vertical phase speed of the shorter waves is observed to decrease quite linearly (except at the altitude of 48 km) between heights of 43 km and 60 km to a minimum of -0.27 m/s. Both aforementioned methods can also be useful to identify structures with an upward and downward phase progression. A downward phase progression is generally observed to be dominant. Lintelman and Gardner (1994) studied the density variance of both waves with a downward and upward phase progression over 50 nights of observation. The variance exhibited a high correlation between waves

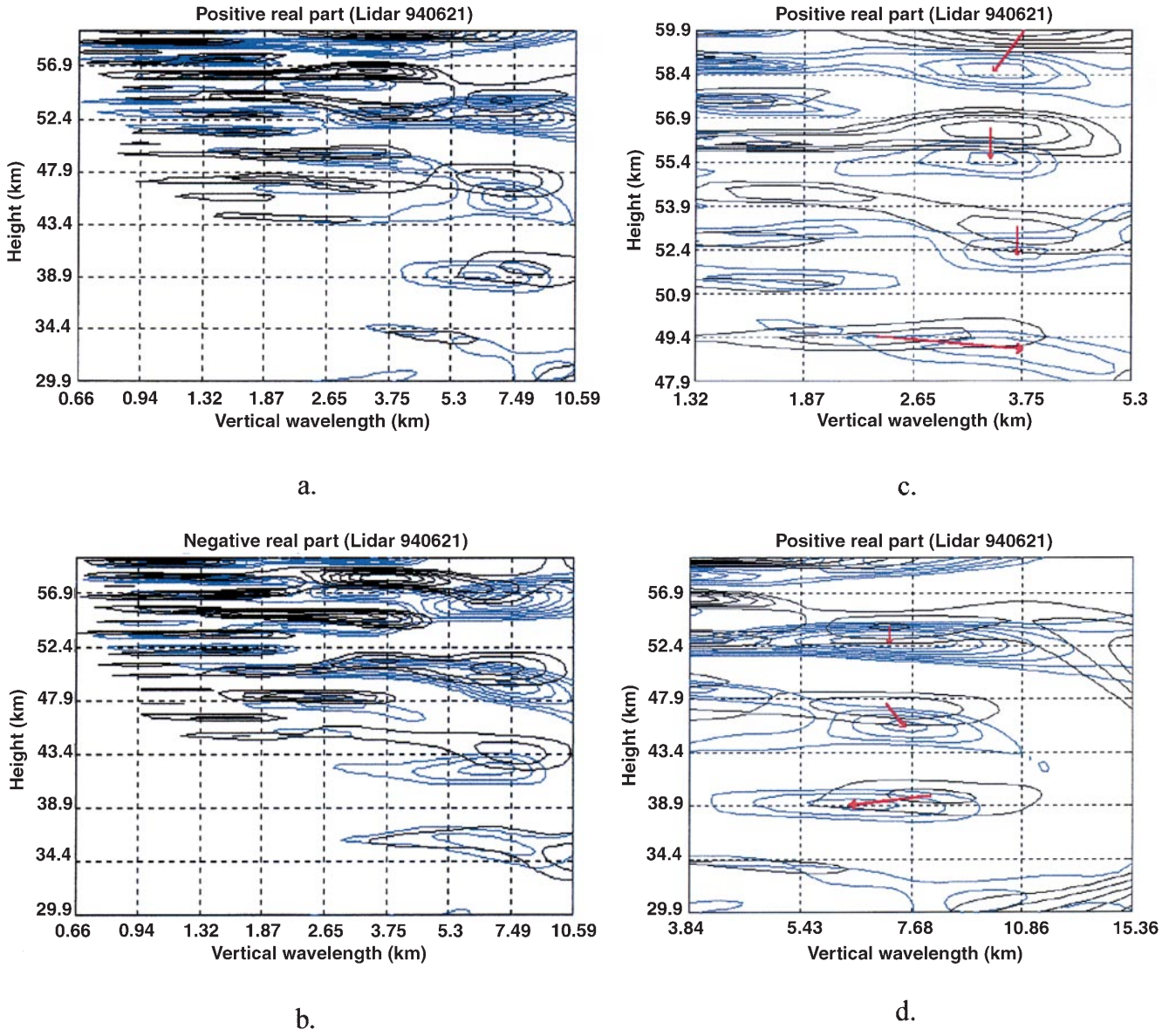

Fig. 6a–d. Contour lines of the CWT real part using the eighth derivative of the Gaussian are superposed for 30-min average profiles 6 and 9 on June 21, 1994, **a** and **b** *black* and *blue contour lines* respectively. Similar patterns are identified for the previous observed waves. **c, d** show zoom-ins for the dominant modes with 3-km and 7-km vertical wavelengths, respectively. The *direction* of the *arrows* indicates a downward phase progression

with an upward and downward phase progression and this suggested that both waves could be generated by a same wave source.

From the estimated values of the vertical wavelengths outside regions which are affected by wave reflection, we obtained observed periods T of about 3 h ($T = \lambda_v/c_z$, $\lambda_v = 3$ km and $c_z = -0.3$ m/s in the lower mesosphere) and 7.5 h ($\lambda_v = 7$ km and $c_z = -0.26$ m/s in the stratopause). By assuming negligible Doppler shifting effects on wave frequency, horizontal phase speeds c_h have absolute values of 8.8 m/s ($c_h = |N/m|$, $N = 1.7 \times 10^{-2}$ rad/s and $\omega/f = 11.5$) and 18 m/s ($\omega/f = 4.5$ and $N = 1.6 \times 10^{-2}$ rad/s) and horizontal wavelengths λ_h of 88 km and 485 km ($\lambda_h = \lambda_v\,|c_h/c_z|$) for the modes with vertical wavelengths of 3 km and 7 km respectively. Values of estimated horizontal parameters are biased in the case of Doppler shifting effects on wave frequency and more particularly when the direction of the background wind and the wave-propagation vectors is identical or opposite.

The wind field (Fig. 4) is characterized by the quasi-biennal oscillation (QBO) with an westward zonal wind ($|\mathbf{u}| < 5$ m/s) in the stratosphere up to 37 km and by the mid-latitude westerlies at the stratopause level with a eastward zonal wind with $|\mathbf{u}| < 20$ m/s at heights between 37 km and 45 km at the latitudes about 21°S during Austral winter in 1994 (Andrews *et al.*, 1987; Marquardt and Naujokat, 1997; Hitchman *et al.*, 1997). Thus waves with $c_h < -5$ m/s and $c_h > 18$ m/s produced at heights ≤10 km can enter the upper stratosphere since

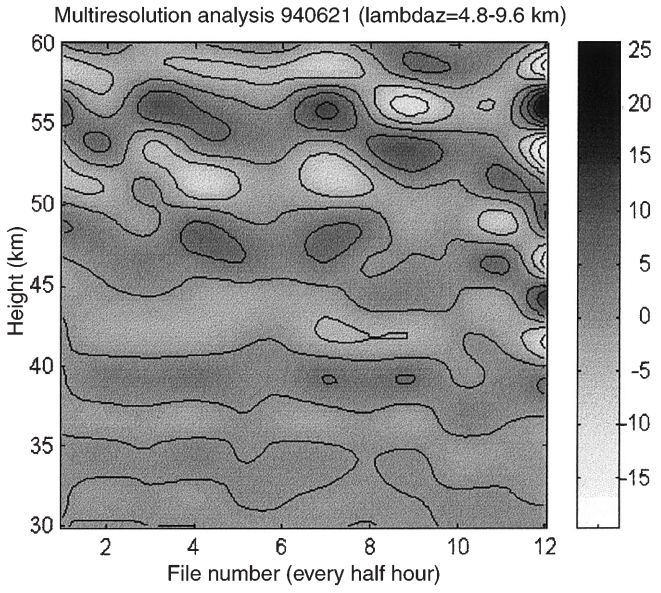

Fig. 7. The time and spatial evolution of the dominant wavelike patterns with 4.8–9.6 km vertical wavelengths (d_4), is derived from the MRA of successive 30-min integrated vertical temperature perturbation profiles for the night of June 21. A negative phase speed appears in the lower mesosphere

they do not encounter critical levels (Eckermann, 1995b). Moreover, the observed periods and the horizontal wavelengths agree well with the distributions of observed periods against horizontal wavelengths obtained at different locations by several instruments. These distributions are listed by Reid (1986), Manson (1990), and more recently by Taylor *et al.* (1997).

5 First climatology

The CWT with the Morlet wavelet is applied to night averaged vertical temperature perturbation profiles for 15 nights of observation from late May to late November in 1994 during Austral winter. The duration of the observation varies between 2.5 and 8.5 h with a mean value of 5 h. During this season, the subtropical jet is more intense and located nearer La Reunion Island. Thus, subtropical conditions are expected due to the fact that most of the measurements were obtained in June. Observed wavelike structures with vertical wavelengths <11 km at altitudes between 30 km and 60 km are extracted by applying the method of the CWT 'skeleton'. Minimum and maximum intensities of the CWT 'skeletons' are then converted to perturbation amplitudes. This conversion is possible thanks to the conservation of the energy of the signal in the space-scale plane through the use of the Morlet CWT. The climatology is carried out on observed quasi-monochromatic wavelike structures with perturbation amplitudes >1 K. The mean minimum and maximum perturbation amplitudes are observed to be steady for the altitudes ranged from 30–40 km, 40–50 km and 50–60 km with respective values of 1.3 ± 0.4 K, 3.4 ± 1.9 K, 1.3 ± 0.4 K, 3.7 ± 2.1 K, 1.2 ± 0.4 K and 3.7 ± 2.1 K.

The histogram of the vertical wavelength distribution (Fig. 9a) shows an evident dominant activity of wavelike structures with 3–4 km vertical wavelengths at the altitudes ranged from 30–60 km. The number of modes present with 4–5 km vertical wavelengths decreases with increasing altitudes. Conversely, the number of modes present with 2–3 km vertical wavelengths increases. Dominant modes with a 2-km vertical wavelength are missing in the upper stratosphere and are observed from the stratopause. In addition, the number of modes present with vertical wavelengths >6 km is observed to increase with increasing altitude.

Generally, two wavelike structures are observed with vertical wavelengths between 3–4 km and >6 km from 30 km in altitude. A third mode with a vertical wavelength <3 km is often observed from the stratopause and might be the result of nonlinear interactions between both the other observed modes. Moreover, wavelike structures with vertical wavelengths near 10 km are present in the lower mesosphere. The histogram of the mean vertical phase speed distribution (Fig. 9b) is obtained by using the MRA for the determination of the vertical phase speed. Values of the phase progression >-0.05 m/s which are observed in the upper stratosphere are not taken into consideration. The histogram shows that mean vertical phase speeds are mainly >-0.3 m/s with a peak at -0.3 m/s. A dominant activity of modes with a downward phase progression between -0.3 and -0.1 m/s is clearly observed from the stratopause. Observed periods are calculated from observed vertical wavelengths and phase speeds (Fig. 9c). The histogram reveals a dominant activity of dominant modes with observed periods <5 h with a peak at 3–4 h and periods of 9 h.

Due to the lack of observational experiments in the Southern Hemisphere, a selection of results of gravity wave parameters (vertical wavelengths, vertical phase speeds) in the mid-latitude, the tropical and the equatorial regions in both hemispheres is reported in Table 2.

The gravity wave parameters over Arecibo (18°N, 67°W) during January, March and April in 1989 reveal a dominant activity of modes with vertical wavelengths between 4 and 8 km in the stratopause and no modes with vertical wavelengths longer than 10 km are observed (Beatty *et al.*, 1992). Our results are also consistent with the vertical wavelengths observed by Fritts *et al.* (1997) in the tropical Southern Hemisphere during the Austral winter period in 1994. Moreover, our study shows the presence of dominant modes with vertical wavelengths between 3 km and 4 km above 40 km in altitude. In addition, results seem to be similar to those mentioned by Gardner *et al.* (1989) at mid-latitudes in Illinois. Their observed periods are estimated between 1.5 h and 17 h with an average value of 4 h. As for the statistical distribution of the vertical wavelengths, Kitamura and Hirota (1989) showed the dominance of 3–5 km gravity waves in the lower stratosphere over Japan in wintertime on the basis of balloon observations. All these different observations are consistent with the fact that our data

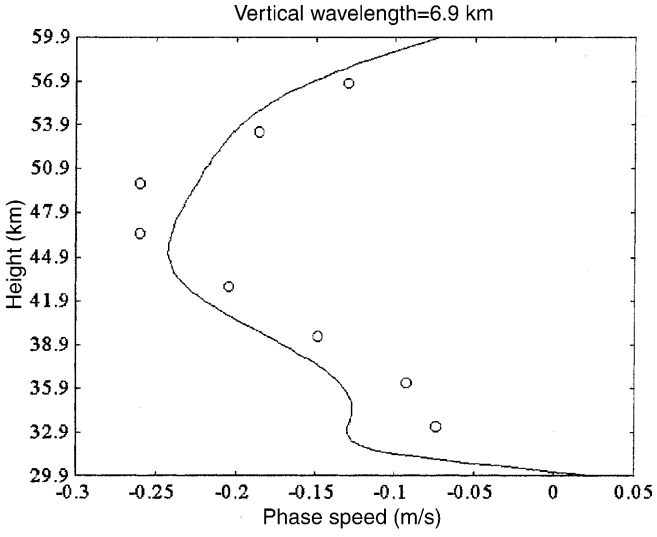

a.

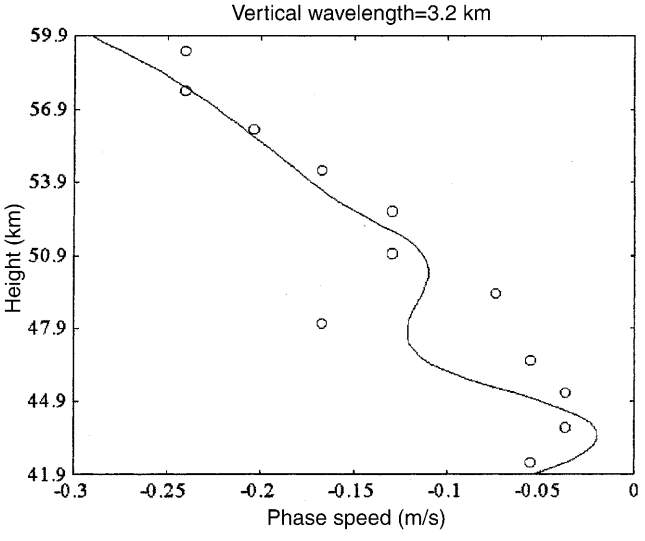

b.

Fig. 8a, b. Phase speed as a function of altitude **a** for the 6.9-km and **b** the 3.2-km vertical wavelengths for 30 min average profiles 6 and 9 on June 21. *Solid lines* and *circles* represent respectively the phase speed derived from phase sections using the Morlet wavelet and from the maximum and minimum amplitudes of the wavelike structure obtained by the use of the eighth derivative of the Gaussian. This last method takes the vertical wavelength variations into account

set corresponds to the Austral winter period with subtropical conditions.

Fritts and Luo (1992) simulated gravity waves which were excited by geostrophic adjustment of the jet stream. Energetic waves near inertial frequency with 6–8 km vertical wavelengths were observed to be vertically radiated far away in the atmosphere. Hostetler and Gardner (1994) suggested that such a source could be

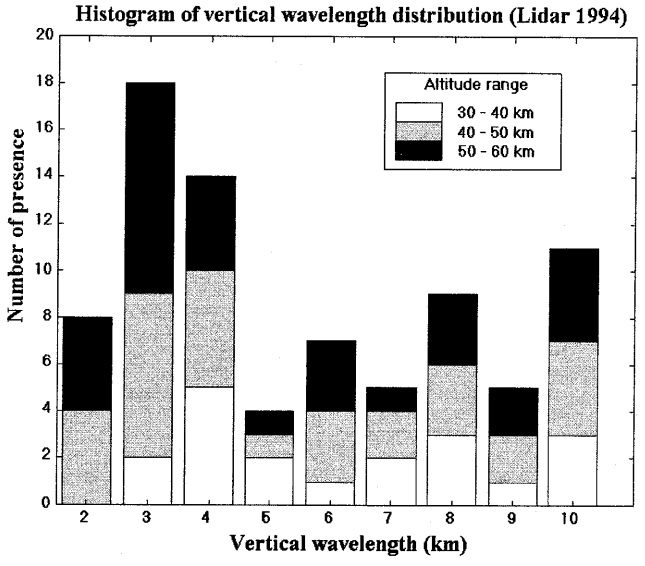

a.

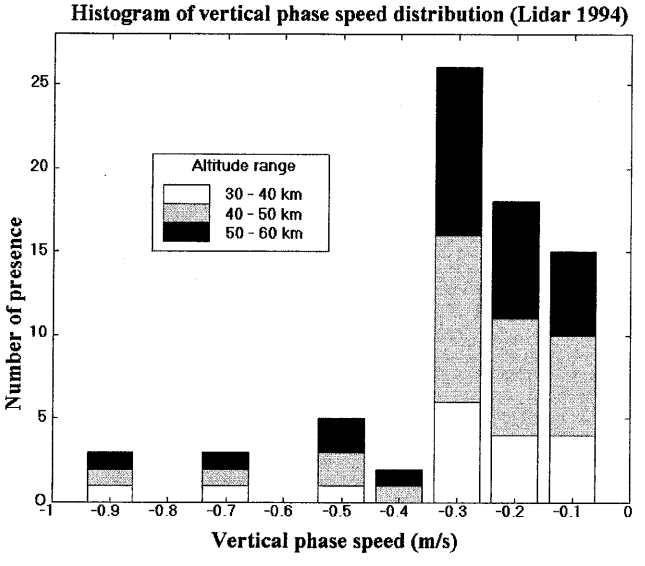

b.

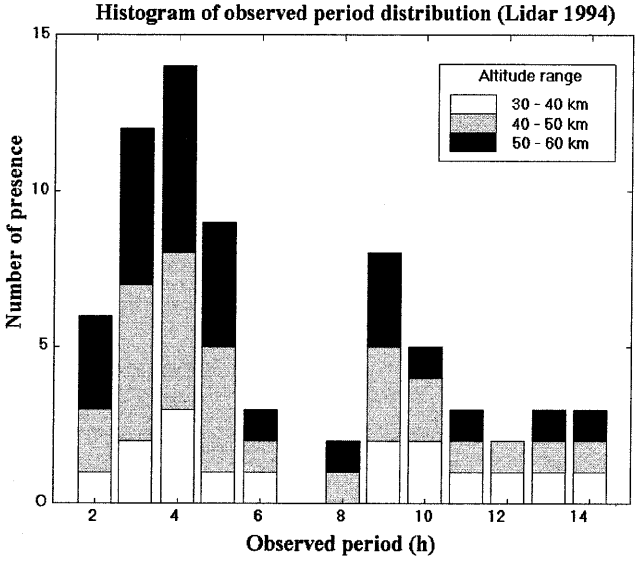

c.

Fig. 9a–c. Distribution of vertical parameters for the altitudes ranged from 30–40 km, 40–50 km and 50–60 km resulting from 15 nights of observation from late May to late November in 1994: **a** vertical wavelengths **b** mean vertical phase speeds, and **c** observed periods

Table 2. A selection of results of gravity wave parameters in mid-latitude, tropical and equatorial regions

References	Locations	Instruments	Experimental data	Height (km)	Dominant λ_v (km)	Observed c_z (m/s)
Michell *et al.* (1994)	UK Aberystwyth (52°N, 4°W)	Lidar Radar MST	September 25, December 13–14 1990, January 21–22 1991	2–50	5–8	−0.2 to −0.4 34–48 km height
Wilson *et al.* (1991)	France Biscarosse (44°N, 1°W) O.H.P. (44°N, 6°E)	Lidar	1986–1989	30–75	5–10	−0.3 at 40 km height
Carswell *et al.* (1991)	Canada Torronto (44°N, 80°W)	Lidar	September–October 1989–1990	30–50	3 10	1–0.7
Gardner and Voelz (1987)	USA Illinois (40°N, 88°W)	Lidar	December 1980–May 1986	85–105	2–17	−0.3 to −1.8
Gardner *et al.* (1989)	USA Illinois (40°N, 88°W)	Lidar	January 1984–November 1986	35–50	2–4 7–10	−0.01 to −0.85
Kwon *et al.* (1990)	USA Colorado Mid-latitudes	Radar Lidar	November 1986	81–89 84–92	8–9 12	−0.19 −1.8
Meriwether *et al.* (1994)	USA Ohio Mid-latitudes	Lidar	July 1989–March 1990	40–90	5–15	−0.1 to −0.7
Qian and Gardner (1995)	USA Illinois (40°N, 88°W)	Lidar Ca Na	December 21–22 1992	85–100	7.6	−0.4 at 88.5–92.5 km height
Kitamura and Hirota (1989)	Japan (40°N, 140°E)	Rawinsondes	1986	15–20	3–5	?
Namboothiri *et al.* (1996)	Japan Shigaraki (35°N, 136°E) Hiachioji (36°N, 139°E)	Radar MU Lidar Na	December 15–16 1993	80–95	16	−0.45
Nakamura *et al.* (1993)	Japan (35°N, 136°E)	Radar MU	1986–1991	70–75	4–15	±0.1 to ±0.4
Gavrilov *et al.* (1997)	Japan Shigaraki (35°N, 136°E)	Radar MU	1987–1988	70–80	8–12	?
Shibata *et al.* (1986)	Japan Fukuoka (33°N, 130°E)	Lidar	March 1985–April 1986	30–60	10	−0.33 to 0
Chane-Ming *et al.* (this study)	Reunion island (21°S, 55°E)	Lidar	May–November 1994	45–60 30–60	≤3 3–4 6–11	−0.35 to −0.05 at 30–60 km height
Beatty *et al.* (1992)	Porto Rico Arecibo (18°N, 67°W)	Lidar	January, March, April 1989	25–55 80–105	2.8–17 1.1–12.8	−2.7 to −0.06
Fritts *et al.* (1997)	Brasil Alcantara (2°S, 45°W)	Rockets Radar	August 1994	27–60 <30 >30	1–3 5–10	?

responsible for energetic vertical waves longer than 6 km observed in the upper stratosphere and the upper mesosphere during the ALOHA-90 experiments in the vicinity of Hawaii (20.8°N, 156.2°W; a northern latitude which corresponds to the southern latitude of La Reunion Island).

6 Summary and conclusions

In conclusion we illustrated some interesting capabilities of the continuous wavelet transform with two Gaussian type 'mother' wavelets and the multiresolution analysis as extracting and analyzing information from vertical temperature perturbation profiles associated with gravity wave structures observed above La Reunion Island. In this work, each method was successively used to yield additional information on the behavior of gravity wave vertical characteristics as a function of altitude and time. The first method (the CWT) produces a continuous analysis in the altitude-wavelength plane which is adequate to a visual interpretation of the signal. The use of two kinds of wavelets such as the Morlet complex-valued wavelet and the eighth derivative of the Gaussian enables

one to provide complementary representations of the information included in the signal. The second method enables a fast decomposition and a perfect reconstruction of the signal over orthonormal bases through filter banks. Our attention focused on the vertical wavelength, the vertical phase speed and the energy distribution. The extraction of CWT spectral lines of a vertical temperature perturbation profile proved to be an easy way to survey the day-to-day variability of such wavelike structures. Moreover, the CWT computation through the Fourier transform enabled us to identify and localize quickly night averaged vertical wavelengths (refer to Sects. 4.1 and 5). The multiresolution decomposition was illustrated and provided a global view of the time and spatial evolution of wavelike structure extrema from the successive 30 min integrated temperature perturbation profiles. Two other complementary methods were presented for estimating the phase progression. These methods were illustrated using the case study of June 21, 1994, and it showed a clear downward phase progression (>-0.3 m/s) of observed wavelike structures with vertical wavelengths <10 km in the stratopause and in the lower mesosphere. A preliminary climatology of observed dominant modes during the Austral winter in 1994 was drawn up. We observed two dominant waves with vertical wavelengths of about 4 km and >6 km on many nights of observations at the altitudes between 30 and 60 km. A third mode with a vertical wavelength <3 km was often observed from the stratopause and might result from nonlinear interactions between the other modes. Observations on the vertical wavelengths, the vertical phase speeds and the periods deduced from the preliminary climatology were consistent with those derived from the case study of June 21. Moreover, as expected, comparisons with gravity wave parameters obtained at other sites showed that our results were in agreement with those observed under subtropical conditions during winter.

The lidar instrument has been improved since late 1994 and now provides other additional measurements from the toposphere to the mesosphere (Bencherif *et al.*, 1996). This study will be extended to a larger data set of which measurements have been recently validated for the NDSC. In particular, this extension will enable the characterization of gravity wave parameters during Austral summer.

Acknowledgements. This work was supported by a grant from La Region Réunion. The authors are grateful to Dr H. Bencherif and G. Bain for acquiring lidar data in 1994 and Dr. G.L. Roff for providing UKMO-UARS assimilated data from BADC. Additional thanks to G. Mégie, Director of the Institut Pierre Simon Laplace for his support to the Laboratoire de Physique de l'Atmosphère, Ms Cardon for the documentation and two anonymous reviewers who provided helpful comments on the manuscript.

Topical Editor F. Vial thanks I. Hirota and another referee for their help in evaluating this paper.

Appendix A: the continuous wavelet transform algorithm

The CWT coefficients (CWT(a,b)) result from the projection of the signal (s) on a set of translated and dilated functions (respectively by the parameters b and a) derived from the 'mother' wavelet (g):

$$CWT(a,b)=\frac{1}{\sqrt{a}}\int s(t)\hat{g}\left(\frac{t-b}{a}\right)\mathrm{d}t=(s*\bar{g}_a)(b) \tag{2}$$

$$\bar{g}_a(t)=\frac{1}{\sqrt{a}}\hat{g}\left(-\frac{t}{a}\right) \tag{3}$$

where a is the scale parameter; b is time translation parameter; *, convolution product;$\hat{}$: conjugaison; s, analyzed signal and g is the 'mother' wavelet.

The CWT coefficients are rapidly computed through the Fourier transform due to the convolution product:

$$CWT(a,b)=FFT^{-1}(\sqrt{a}FFT(s(t))\cdot\overline{FFT}(g(t))_{\omega=a\omega}) \tag{4}$$

FFT is the fast Fourier transform and ω, the frequency variable.

Mathematical formulations of the wavelets and the associated Fourier transforms used in this study for the computation of the CWT include:

The Morlet complex-valued wavelet

$$\begin{aligned} g_{\omega_o}(t)&=\mathrm{e}^{i\omega_o t}\mathrm{e}^{-\frac{t^2}{2}}\\ g(\omega)&=\mathrm{e}^{-\frac{(\omega-\omega_0)^2}{2}}\end{aligned}\quad\text{with}\quad \omega_o=\pi\sqrt{\frac{2}{2\ln 2}}\approx 5.336\ , \tag{5}$$

and *the eighth derivative of the Gaussian.*

The nth order derivatives of the Gaussian are given by the following equations (Grossmann, 1988):

$$g^{(n)}(t)=\frac{\mathrm{d}^n\mathrm{e}^{-\frac{t^2}{2}}}{\mathrm{d}t^n}=(-1)^n He_n\mathrm{e}^{-\frac{t^2}{2}}$$

$$\text{with } He_n(t)=2^{-\frac{n}{2}}H_n\left(\frac{t}{\sqrt{2}}\right)\quad H_n:\text{ Hermite polynomial} \tag{6}$$

$$\text{and } g^{(n)}(\omega)=(-1)^n n(i\omega)^n\ \mathrm{e}^{-\frac{\omega^2}{2}}$$

The eighth derivative of the Gaussian uses the following expressions:

$$g(t)=(t^8-28t^6+210t^4-405t^2+90)\mathrm{e}^{-\frac{t^2}{2}}$$

$$g(\omega)=\omega^8\mathrm{e}^{-\frac{\omega^2}{2}} \tag{7}$$

(the multiplicative constants are not mentioned).

Appendix B: the multi-resolution analysis, the pyramid algorithm

The series of approximations and details of ($a(n)$) and ($d(n)$) for scale level 1 (at scale 2^{-1}) are calculated here by applying analysis and synthesis operators (Fig. 10a) to the digital signal ($s(n)$):

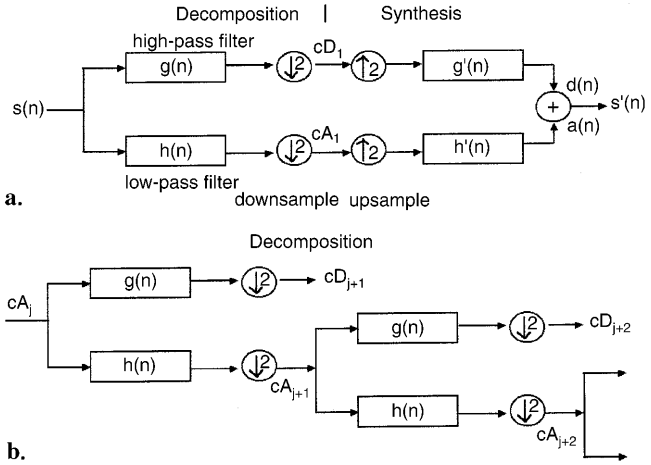

Fig. 10a, b. Pyramid scheme (or the Mallat algorithm) of the MRA. **a** Decomposition and synthesis of the signal ($s(n)$); g and h (g' and h') are the analysis (synthesis) FIR filters, cD_1, and cA_1 denote respectively the detail and approximation coefficients at level 1. **b** Decomposition of the signal ($s(n)$) from level j to $j+2$

Table 3. The DB8 coefficients associated with analysis FIR filters ($h(n)$) and ($g(n)$)

n	$h(n)$	$g(n)$
0	−0.000117476784	−0.054415842243
1	0.000675449406	0.312871590914
2	−0.000391740373	−0.675630736297
3	−0.004870352993	0.585354683654
4	0.008746094047	0.015829105256
5	0.013981027917	−0.284015542962
6	−0.04408825393	−0.0004724845745
7	−0.017369301002	0.128747426620
8	0.128747426620	0.017369301002
9	0.0004724845745	−0.04408825393
10	−0.284015542962	−0.013981027917
11	−0.015829105256	0.008746094047
12	0.585354683654	0.004870352993
13	0.675630736297	−0.000391740373
14	0.312871590914	−0.000675449406
15	0.054415842243	−0.000117476784

1. The analysis FIR filters ($h(n)$ and $g(n)$) by convolution followed by a downsampling for the decomposition;
2. Then an upsampling and the synthesis FIR filters ($h'(n)$ and $g'(n)$) by convolution for the reconstruction

The FIR filters ($h(n)$ and $g(n)$) correspond respectively to a low-pass and high pass filter (m_0 and m_1) in the Fourier space and to the scaling function and the wavelet respectively in the direct space.

The synthesis filters ($h'(n)$ and $g'(n)$) are chosen to produce a perfect reconstruction and can be obtained by transposing the analysis FIR filters.

After each spilt (Fig. 10b), the downsampling operation ensures a decrease by twice the number of the detail and the approximation coefficients (cA and cD). For the synthesis, the odd-numbered components are returned as zeros by an upsampling.

Table 3 gives the DB8 coefficients of the analysis FIR filters ($h(n)$ and $g(n)$) used in this study.

References

Alexander, M. J., Interpretations of observed climatological patterns in stratospheric gravity wave variance, *J. Geophys. Res.*, **103,** 8627–8640, 1998.

Allen, S. J., and R. A. Vincent, Gravity wave activity in the lower atmosphere: Seasonal and latitudinal variations, *J. Geophys. Res.*, **100,** 1327–1350, 1995.

Ambardar, A., *Analog and digital signal processing*, PWS Publishing, Boston 1995.

Andrews. D. G., J. R. Holton, and C. B. Leovy, *Middle atmosphere dynamics*, Academic Press, New York 1987.

Bacmeister, J. T., S. D. Eckermann, P. A. Newman, L. Lait, K. R. Chan, M. Loewenstein, M. H. Proffitt, and B. L. Gary, Stratospheric horizontal wave number spectra of winds, potential temperature and atmospheric tracers observed by high-altitude aircraft, *J. Geophys. Res.*, **101,** 9441–9470, 1996.

Barcelo, A., R. Robert, and J. Coudray, A major rainfall event: the 27 February–5 March 1993 rains on the southeastern slope of Piton de la Fournaise massif (Reunion Island, Southwest Indian Ocean), *Mon Weather Rev.*, **125,** 3341–3346, 1997.

Beatty, T. J., C. A. Hostetler, and C. S. Gardner, Lidar observations of gravity waves and their spectra near the mesopause and stratopause at Arecibo, *J. Atmos. Sci.*, **49,** 477–496, 1992.

Bencherif, H., J. Leveau, J. Porteneuve, P. Keckhut, A. Hauchecorne, G. Mégie, and M. Bessafi, Lidar developments and observations over Réunion Island (20°S, 55.5°E) in *Advances in Atmospheric Remote Sensing with Lidar*, *18th International Laser Radar Conference*, Eds. A. Ansmann, R. Neuber, P. Rairoux, V. Wandiger, 553–556, 1996.

Carswell, A. I., S. R. Pal, W. Steinbrecht, J. A. Whiteway, A. Ulitsky, and T. Y. Wang, Lidar measurements of the middle atmosphere, *Can. J. Phys.*, **69,** 1076–1086, 1991.

Chane-Ming, F., Analyse de signaux géophysiques dans l'atmosphére par les techniques en ondelettes: Etude des ondes de gravité en région tropicale, Thése de doctorat de l'Université de la Réunion, Dec., 1998.

Chane-Ming, F., F. Molinaro, and J. Leveau, Gravity wave activity in the southern intertropical middle atmosphere by wavelet analysis, *Proceedings of the First SPARC General Assembly*, 275–278, 1997a.

Chane-Ming, F., F. Molinaro, and J. Leveau, Applications de l'analyse en ondelettes sur un signal géophysique, *Seiziéme Colloque GRETSI*, 1013–1016, 1997b.

Chanin, M. L., and A. Hauchecorne, Lidar observation of gravity and tidal waves in the stratosphere and mesosphere, *J. Geophys. Res.*, **86,** 9715–9721, 1981.

Connor, L. N., and S. K. Avery, A three-year gravity wave climatology of the mesosphere and lower thermosphere over Kauai, *J. Geophys. Res.*, **101,** 4065–4077, 1996.

Daubechies, I., The wavelet transform, time-frequency localization and signal analysis, *IEEE Trans. Inform. Theor.,* **36,** 961–1005, 1990.

Daubechies, I., Ten lectures on wavelets, *CBMS-NSF Regional Conference Series in Applied Mathematics*, 1992.

Demoz, B. B., D. O'C. Starr, K. R. Chan, and S. W. Bowen, Wavelet analysis of dynamical processes in cirrus, *Geophys. Res. Lett.*, **25,** 1347–1350, 1998.

Eckermann, S. D., On the observed morphology of gravity-wave and equatorial-wave variance in the stratosphere, *J. Atmos. Terr. Phys.*, **57,** 105–134, 1995a.

Eckermann, S. D., Effect of background winds on vertical wavenumber spectra of atmospheric gravity waves, *J. Geophys. Res.,* **100,** 14 097–14 112, 1995b.

Eckermann, S. D., I. Hirota, and W. K. Hocking, Gravity wave and equatorial wave morphology of the stratosphere derived from long-term rocket sounding. *Q. J. R. Meteorol. Soc.*, **121,** 149–186, 1995.

Farge, M., Wavelet transforms and their applications to turbulence, *Annu. Rev. Fluid Mech.*, **24,** 395–457, 1992.

Fritts, D. C., Gravity waves in the middle atmosphere of the southern hemisphere, in *Dynamics, transport and photochemistry in the middle atmosphere of the southern hemisphere*, Kluwer Academic Publishers, Dordrecht, 171–189, 1990.

Fritts, D. C., and Z. Luo, Gravity wave excitation by geostrophic adjustment of the stream. Part I: two-dimensional forcing. *J. Atmos. Sci.*, **42,** 681–697, 1992.

Fritts, D. C., J. F, Carten, D. M. Riggin, R. A. Golberg, G. A. Lehmacher, F. J. Schmidlin, S. McCarthy, E. Khudeki, C. D. Fawcett, M. H. Hitchman, R. S. Lieberman, I. M. Reid, and R. A. Vincent, Equatorial dynamics observed by rocket, radar, and satellite during the CADRE/MALTED campaign 2. Mean and wave structures, coherence, and variability, *J. Geophys. Res.*, **102,** 26 191–26 216, 1997.

Gardner, C. S., and D. G. Voelz, Lidar studies of the night sodium layer over Urbana, Illinois. 2. Gravity waves, *J. Geophys. Res.*, **92,** 4673–4694, 1987.

Gardner, C. S., M. S. Miller, and C. H. Liu, Rayleigh lidar observations of gravity wave activity in the upper stratosphere at Urbana, Illinois, *J. Atmos. Sci.*, **46,** 1838–1854, 1989.

Gavrilov, N. M., S. Fukao, T. Nakamura, and T. Tsuda, Statistical analysis of gravity waves observed with the middle and upper radar in the middle atmosphere 2. Waves propagated in different directions, *J. Geophys. Res.*, **102,** 13 433–13 440, 1997.

Gill, A. E., Atmosphere-ocean dynamics, Academic, Press New York, 1982.

Grossmann, A., Wavelet transforms and edge detection, in *Stochastic Processes in Physics and Engineering*, D. Reidel Dordrecht, 149–157, 1988.

Hamilton, K., Climatological statistics of stratospheric inertia-gravity waves deduced from historical rocketsonde wind and temperature data, *J. Geophys. Res.*, **96,** 831–839, 1991.

Hauchecorne, A., and M. L. Chanin, Density and temperature profiles obtained by lidar between 35 and 70 km, *Geophys. Res. Lett.*, **7,** 565–568, 1980.

Hauchecorne, A., M. L. Chanin, P. Keckhut, and D. Nedeljkovic, Lidar monitoring of the temperature in the middle and lower atmosphere, *Appl. Phys. B*, **55,** 29–34, 1992.

Hines, C. O., Internal atmospheric gravity waves at ionospheric heights, Can. *J. Phys.*, **38,** 1441–1481, 1960.

Hirota, I., Climatology of gravity waves in the middle atmosphere, *J. Atmos. Terr. Phys.*, **46,** 767–773, 1984

Hitchman, M. H., E. Kudeki, D. C. Frittis, J. M. Kugi, C. Fawcett, G. A. Postel, C-Y. Yao, D. Ortland, D. Riggin, and V. Lynn Harvey, Mean winds in the tropical stratosphere during January 1993, March 1994, and August 1994, *J. Geophys. Res.*, **102,** 26 033–26 051, 1997.

Holton, J. R., The dynamic meteorology of the stratosphere and mesosphere, American Meteorological Society, Meteorology Monograph 37, 1975.

Hostetler, C. A., and C. S. Gardner, Observations of horizontal and vertical wave number spectra of gravity wave motion in the stratosphere and mesosphere over the mid-Pacific, *J. Geophys. Res.*, **99,** 1283–1302, 1994.

Isler, J. R., M. J. Taylor, and D. C. Fritts, Observational evidence of wave ducting and evanescence in the mesosphere, *J. Geophys. Res.*, **102,** 26 301–26 313, 1997.

Keckhut, P., M. L. Chanin, and A. Hauchecorne, Stratosphere temperature measurement using Raman lidar, *Appl. Optics*, **29,** 5182–5186, 1990.

Keckhut, P., A. Hauchecorne, and M. L. Chanin, A critical review of the database acquired for the long-term surveillance of the middle atmosphere by the French Rayleigh lidars, *J. Atmos. Ocean. Technol.* **10,** 850–867, 1993.

Kitamura, Y., and I. Hirota, Small-scale disturbances in the lower stratosphere revealed by daily rawinsonde observations, *J. Meteorol. Soc. Japan*, **67,** 817–831, 1989.

Kuo, F. S., and H. Y. Lue, Effect of the wave-shear interaction on gravity wave activity in the lower and middle atmosphere, *J. Atmos. Terr. Phys.*, **56,** 1147–1155, 1994.

Kurylo, M. J., and S. Solomon, Network for the detection of stratospheric change, NASA Report, Code EEU, 1990.

Kwon, K. H., C. S. Gardner, S. K. Avery, and J. P. Avery, Correlative radar and airborne sodium lidar observations of the vertical and horizontal structure of gravity waves near the mesopause, *J. Geophys. Res.*, **95,** 13, 737–748, 1990.

Lindzen R. S., Turbulence and stress owing to gravity wave and tidal breakdown, *J. Geophys. Res.*, **86,** 9707–9714, 1981.

Lintelman, S. A., and C. S. Gardner, Observation and interpretation of spectra of atmospheric gravity wave perturbations with upward and downward phase progression, *J. Geophys. Res.*, **99,** 959–971, 1994.

Marquardt, C., and B. Naujokat, An update of the equatorial QBO and its variability, *Proc. First SPARC General Assembly*, 87–90, 1997.

Manson, A. H., Gravity wave horizontal and vertical wavelengths: An update of measurements in the mesopause region (~80–100 km), *J. Atmos. Sci.*, **47,** 2765–2773, 1990

McLandress, C., On the importance of gravity waves in the middle atmosphere and their parameterization in general circulation models, *J. Atmos. Terr. Sol. Phys.*, **60,** 1357–1383, 1998.

Meriwether, J. W., P. D. Dao. R. T. McNutt, W. Klemetti, W. Moskowitz, and G. Davidson, Rayleigh lidar observations of mesosphere temperature structure, *J. Geophys. Res.*, **99,** 973–987, 1994.

Mitchell, N. J., L. Thomas, and I. T. Prichard, Gravity waves in the stratosphere and troposphere observed by Lidar and MST radar, *J. Atmos. Terr. Phys.*, **56,** 939–947, 1994.

Nakamura, T., T. Tsuda, M. Yamamoto, S. Fukao, and S. Kato, Characteristics of gravity waves in the mesosphere observed with the middle and upper atmosphere radar. 2. Propagation direction, *J. Geophys. Res.*, **98,** 8911–8923, 1993.

Namboothiri, S. P., T. Tsuda, M. Tsutsumi, and T. Nakamura, Simultaneous observations of mesospheric gravity waves with the MU radar and a sodium lidar, *J. Geophys. Res.*, **101,** 4057–4063, 1996.

Qian, J., and C. S. Gardner, Simultaneous lidar measurements of mesospheric Ca, Na, and temperature profiles as Urbana, Illinois, *J. Geophys. Res.*, **100,** 7453–7461, 1995.

Reid, I. M., Gravity wave motions in the upper middle atmosphere (60–110 km), *J. Atmos. Terr. Phys.*, **48,** 1057–1072, 1986.

Rioul, O., and M. Vetterli, Wavelets and signal processing, *IEEE Signal Processing Mag.*, 14–38, 1991.

Salby, M. L., Fundamentals of atmospheric physics, Academic Press New York, 1995.

Sato, K., and M. Yamada. Vertical structure of atmospheric gravity waves revealed by the wavelet analysis, *J. Geophys. Res.*, **99,** 20 623–20 631, 1994.

Sato, K., T. Kumakura, and M. Takahashi, Gravity waves appearing in a high-resolution GCM simulation. *J. Atmos. Sci.*, **56,** 1005–1018, 1999.

Shibata, T., T. Fukuda, and M. Maeda, Density fluctuation in the middle atmosphere over Fukuoaka observed by a XeF Rayleigh lidar, *Geophys. Res. Lett.*, **13,** 1121–1124, 1986.

Strang, G., and T. Nguyen, *Wavelets and filter banks*, Wellesley-Cambridge Press, Wellesley, USA 1996.

Tannhauser, D. S., and J. L. Attié, Linear analysis of the wave field during a lee wave event of PYREX campaign, *Meteorol. Z.*, N.F.4 203–208, 1995.

Taylor, M. J., W. R. Pendleton Jr., S. Clark, H. Takahashi, D. Gobbi, and R. A. Golberg, Image measurements of short-period gravity waves at equatorial latitudes, *J. Geophys. Res.*, **102,** 26 283–26 299, 1997.

The MathWorks, *Signal processing toolbox user's guide*, The MathWorks, Inc., 1998.

Torrence, C., and G. P. Compo, A practical guide to wavelet analysis, *Bull. Am. Meteorol. Soc.*, **79,** 61–78, 1998.

Torrésani, B., Analyse continue par ondelettes, *Savoirs actuels*, InterEditions/CNRS Editions, Paris 1995.

Tsuda, T., Y. Murayama, T. Nakamura, R. A. Vincent, A. H. Manson, C. E. Meek, and R. L. Wilson, Variations of gravity wave characteristics with height, season and latitude revealed by comparative observations, *J. Atmos. Terr. Phys.*, **56,** 555–568, 1994.

Vanneste, J., and F. Vial, On the nonlinear interactions between gravity waves in shear flows, *NATO ASI Series*, vol I 50, 199–215, 1997.

Vincent, R. A., Gravity-wave motions in the mesosphere, *J. Atmos. Terr. Phys.*, **46,** 119–128, 1984.

Vincent, R. A., Gravity waves in the southern hemisphere middle atmosphere: a review of observations, in *Dynamics, transport and photochemistry in the middle atmosphere of the Southern Hemisphere*, Kluwer Academic Publishers, 159–170, 1990.

Wilson, R., M. L. Chanin, and A. Hauchecorne, Gravity waves in the middle atmosphere observed by Rayleigh lidar: 1. Case studies, *J. Geophys. Res.*, **96,** 5153–5167, 1991.

Wu, D. L., and J. W. Waters, Observations of gravity waves with the UARS microwave limb sounder, *NATO ASI Series*, **I 50,** 103–120, 1997.